Biochemistry

Open Access
This article is licensed under CC-BY 4.0

pubs.acs.org/biochemistry Article

H-cluster Intermediates and Catalytic Properties of *Clostridium pasteurianum* [FeFe]-Hydrogenase III

Effie C. Kisgeropoulos,[⊥] Michael W. Ratzloff,[⊥] Ekaterina M. Stroeva-Dahl, Sarah Hasan,[⊥] Febin Varghese, Jacob H. Artz,[⊥] John W. Peters, David W. Mulder,* and Paul W. King*

Cite This: *Biochemistry* 2025, 64, 2455−2466 Read Online

ACCESS | Metrics & More | Article Recommendations | Supporting Information

ABSTRACT: [FeFe]-Hydrogenases are structurally diverse enzymes that catalyze reversible H_2 activation at a catalytic cofactor or H-cluster. The H-cluster is a [4Fe-4S] cubane linked by a cysteine thiolate to a diiron subsite containing unique CO, CN^-, and dithiomethylamine ligands. The established H-cluster resting state of $[4Fe\text{-}4S]^{2+}$-$[Fe^{II}\text{-}Fe^{I}]$, or H_{ox}, functions in H_2 binding and oxidation, or by proton-coupled reduction initiates H_2 evolution. In contrast, in *Clostridium pasteurianum* [FeFe]-hydrogenase III (CpIII) the resting state of the H-cluster is fully oxidized, $[4Fe\text{-}4S]^{2+}$-$[Fe^{II}\text{-}Fe^{II}]$, or H_{ox+1}. To begin to understand if H_{ox+1} has a role in the mechanism of CpIII, we determined the spectroscopic and redox properties of CpIII H-cluster states under catalytic conditions. CpIII poised in H_{ox+1} and either equilibrated under 1 atm of H_2 or reduced with sodium dithionite, resulted in a mixture of reduced states including H_{ox} ($E_m{}^8 = -407$ mV), H_{trans}-like $[4Fe\text{-}4S]^{+}$-$[Fe^{II}\text{-}Fe^{II}]$ ($E_m{}^8 = -418$ mV), H_{red} $[4Fe\text{-}4S]^{+}$-$[Fe^{II}\text{-}Fe^{I}]$, and H_{redH+} $[4Fe\text{-}4S]^{2+}$-$[Fe^{I}\text{-}Fe^{I}]$ ($E_m{}^8 = -455$−480 mV). Under H_2 the population of the H_{trans}-like state was >20-fold higher than H_{ox}, implicating a role in CpIII catalysis. Unlike other enzymes, there was no spectral evidence of fully reduced states, such as H_{sredH+} ($[4Fe\text{-}4S]^{+}$-$[Fe^{I}\text{-}Fe^{I}]$) or H_{hyd} ($[4Fe\text{-}4S]^{+}$-$[Fe^{II}\text{-}Fe^{II}]$-H^-). Thus, while the H-cluster states of CpIII encompass most of the catalytic intermediates, it is either unable to form H_{sredH+} and H_{hyd}, or these states are highly destabilized in CpIII. Thus, these results demonstrate that catalytic intermediates of reduced CpIII differ from the typical intermediates of other catalytic [FeFe]-hydrogenases and may explain the catalytic preference for H_2 production.

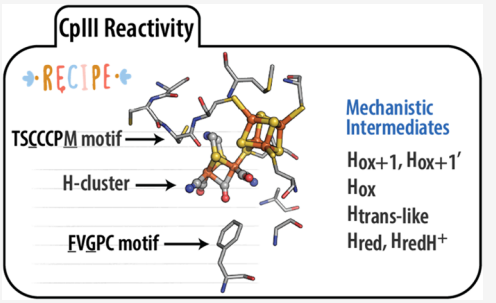

INTRODUCTION

Hydrogenases are enzymes that catalyze reversible H_2 activation—coupled to the oxidation−reduction of electron carrier molecules—to function in energy metabolism and microbial pathogenicity.[1] The [FeFe]-hydrogenases are distinguished by having a conserved, organometallic cofactor, termed the H-cluster, which functions as the site of H_2 activation.[2] The H-cluster is composed of a [4Fe-4S] subsite linked by a cysteine thiolate to a diiron [2Fe] subsite.[3,4] Defining features of the diiron subsite are CO and CN ligands that stabilize each Fe as low-spin Fe^I/Fe^{II} and a bridging dithiol-dimethylamine ligand that functions in proton transfer.[5] In addition to the H-cluster, many [FeFe]-hydrogenases contain diverse complements of accessory iron−sulfur clusters (F-clusters) that mediate the exchange of electrons with external redox partners.

The range of reactivities observed among different classes of [FeFe]-hydrogenases have been hypothesized to result from variations possibly in the secondary coordination environment of the H-cluster (Figure 1),[6,7] or in the nature of the F-clusters.[8−13] Support for the role of the H-cluster environment comes from studies on a variety of engineered enzyme variants,[7,14−18] one example being *Clostridium pasteurianum* [FeFe]-hydrogenase III (CpIII).[6,19,20] Extensive sequence alignment studies of [FeFe]-hydrogenases have led to classification into four main phylogenetic groups, A−D.[2,14,21−26] CpIII is classified as a Group B [FeFe]-hydrogenase, which differs from more well-studied Group A enzymes in the sequence composition of the H-domain that coordinates the H-cluster (Figure 1). For example, CpIII has a TSCCCP H-cluster binding motif versus a more standard TSCCP motif.[6,14,24] The additional cysteine, C221, is located near the surface and C222, the proton-transfer cysteine, is located within hydrogen bonding distance to the H-cluster [2Fe] subsite (Figure 1).[27−29] A CpIII variant with a deletion of C_{223}, which in a CpIII AlphaFold model is expected to coordinate to the H-cluster [4Fe-4S] (Figure 1), resulted in a functional enzyme with attenuated electrochemical activity, demonstrating the importance of the additional cysteine residue to catalysis.[19]

Received: February 3, 2025
Revised: April 8, 2025
Accepted: May 5, 2025
Published: May 13, 2025

Downloaded via NATL RENEWABLE ENERGY LABORATORY on June 5, 2025 at 18:23:17 (UTC).
See https://pubs.acs.org/sharingguidelines for options on how to legitimately share published articles.

© 2025 The Authors. Published by American Chemical Society

https://doi.org/10.1021/acs.biochem.5c00066
Biochemistry 2025, 64, 2455−2466

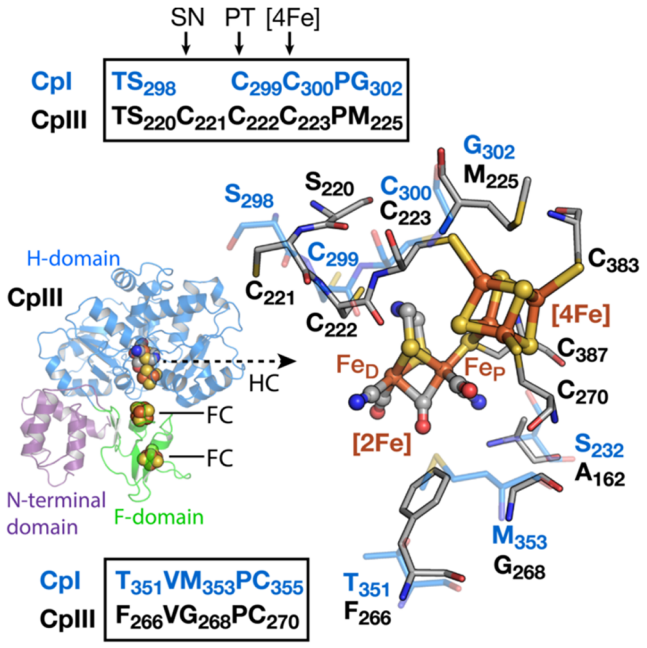

Figure 1. AlphaFold/AlphaFill structural model of CpIII and H-cluster binding region (black) superimposed onto the structure of CpI (blue, PDB ID 3C8Y). The CpIII F-domain (green) coordinates two accessory [4Fe-4S] clusters (FCs), and the H-domain (blue) coordinates the H-cluster (HC). H-cluster motif 1 (**top**) encodes the conserved Cys residues that function in coordination with the cubane subsite ([4Fe], C_{223}) and proton-transfer (PT, C_{222}). The model predicts that C_{221} is a supernumerary cysteine (SN). M_{225} of CpIII is predicted to occupy the same position as G_{302} of CpI to form a part of the electrostatic field near the [4Fe] subsite. Motif 2 (**bottom**) includes residues that form part of the electrostatic field of the diiron subsite ([2Fe]; F_D, distal Fe of [2Fe]; Fe_P, proximal Fe of [2Fe]). The F_{266}/G_{268} pair of CpIII aligns with the T_{351}/M_{353} pair of CpI, which results in an exchange of a polar CH_2SCH_3 side chain of M_{353} for a hydrophobic phenyl ring of F_{266} near the μ-CO of the diiron subsite of the H-cluster. The exchange of A_{162} of CpIII for S_{232} of CpI results in the loss of an H-bond interaction with the CN ligand proximal to the [4Fe] subsite in CpIII. Atomic coloring scheme: C, blue (CpI); C, gray (CpIII); N, blue; O, red; Fe, rust; S, yellow.

Along with the unique TSCCCP motif, variations in the residues of the other H-cluster motifs of CpIII further alter the outer coordination spheres of the two subsites (Figures 1 and S1). It has been hypothesized that these differences collectively alter the dielectric environment of the H-cluster in CpIII to impact stabilities of catalytic states.[6] A striking example of this effect is that the resting state of CpIII is the most oxidized H-cluster state, $[4Fe\text{-}4S]^{2+}$-$[Fe^{II}\text{-}Fe^{II}]$ (or H_{ox+1}).[6] H_{ox+1} shares the same formal oxidation state as the H_{inact} state observed in Group A enzymes from *Desulfovibrio desulfuricans* (DdH) and *Clostridium beijerinckii* (CbA5H),[30−33] and "State 1" that is observed in proton-transfer variants of the H_2 sensing enzyme HydS from *Thermoanaerobacter mathranii* (*Tam*HydS).[34] Both H_{inact} and State 1 are electron paramagnetic resonance spectroscopy (EPR) silent ($S = 0$) with H_{inact} assigned as a noncatalytic state. For DdH and CbA5H, the formation of H_{inact} is accompanied by reversible binding of an S-ligand at the [2Fe] subsite.[16,30,32,35−39] It can also form in synthetically matured DdH by the irreversible binding of free CN^- that is a product of inefficient chemical reconstitution with artificial diiron compounds, or by the addition of a chemical CN^- donor.[40]

For CpIII, the H_{ox+1} state, is observed as the resting state of the recombinant, biosynthesized enzyme,[41−44] isolated under anaerobic, reducing conditions,[6] in the absence of sodium sulfide. Biosynthesis employs the natural maturase machinery for high-fidelity H-cluster synthesis, which unlike reported for chemical reconstitution,[40] sequesters both CO and CN^- as protein-coordinated diiron precursors.[25,26,41,44−48] Because H_{ox+1} is stabilized at potentials of ∼ −400 mV vs NHE) that are similar to the noncatalytic H_{inact} state of CbA5H (E_0 = −383 mV vs NHE),[6,30] raises the question of the role of H_{ox+1} in CpIII and the nature of the reduced states that comprise the catalytic cycle.

Herein, we tested this hypothesis of mechanistic plasticity by examining the reduced states of CpIII using electron EPR and Fourier transform infrared (FTIR) spectroscopy. Specifically, we examined the identity and reduction potentials of H-cluster intermediates in CpIII poised under catalytic conditions. We also tested whether the predicted proton transfer cysteine, C222, was involved in stabilizing the H_{ox+1} state, as demonstrated in CbA5H, by changing Cys to a Ser. The collective results demonstrate that CpIII stabilizes H-cluster oxidation states differently than the Group A [FeFe]-hydrogenases. How these differences may account for the unique reactivity of CpIII is discussed and signifies an underlying role of the coordination sphere in controlling the catalytic properties of the cofactor.

MATERIALS AND METHODS

Enzyme Modeling. The AlphaFold 2 model of *C. pasteurianum* CpIII (A0A0H3J7C7)[49,50] was used in AlphaFill[51] at the 25% identity threshold to populate H- and F-cluster positions. The resulting structure contained multiple possibilities for F-cluster locations. Based on manual inspection of cluster placement chains, only chains U and N were retained as the F-clusters, as they best fit the position of the accessory iron−sulfur cluster sequence motifs in the F-domain of CpIII. Positioning of the diiron site of the H-cluster ($[2Fe]_H$) was further based on superimposition of $[2Fe]_H$ from the X-ray crystal structure of [FeFe]-hydrogenase CpI (PDB ID 3C8Y).[52]

Enzyme Expression and Purification. CpIII (Genbank accession number, WP_003447632) was expressed and purified as previously described and stored anaerobically at 4 °C until usage.[6,20] The CpIII C222S variant construct was generated from the pETDuet-1 CpIII plasmid by site-directed mutagenesis (GeneScript). Expressions and purifications were performed as described previously,[6] and analyzed by SDS-PAGE. Concentrations were determined by Bradford assay. Specific activities of purified enzymes were assayed by H_2 evolution from sodium dithionite-reduced methyl viologen (MV).[6] The CpIII C222S variant displayed a ∼10-fold lower activity than native at 30 μmol H_2 min^{-1} mg^{-1} compared to 305 ± 58 μmol H_2 min^{-1} mg^{-1},[6] consistent with the effect of the Cys-to-Ser exchange of proton-transfer residue in other [FeFe]-hydrogenases.[20]

FTIR and EPR Sample Preparation. *FTIR.* Auto-oxidized (AO) CpIII (Figures 2, 3, 5, and S2) was prepared by G-25 buffer exchange into 50 mM Tris pH 8, 200 mM NaCl, and 5% glycerol and stored at 4 °C. Thionine oxidation of CpIII was carried out by treatment of the as-isolated enzyme by a 1 mM final concentration of thionine (Figure 5). Treatments with either 100% H_2 or D_2 for FTIR (Figure 3) were performed by headspace exchange using 10 vacuum/sparge cycles on a

https://doi.org/10.1021/acs.biochem.5c00066
Biochemistry 2025, 64, 2455−2466

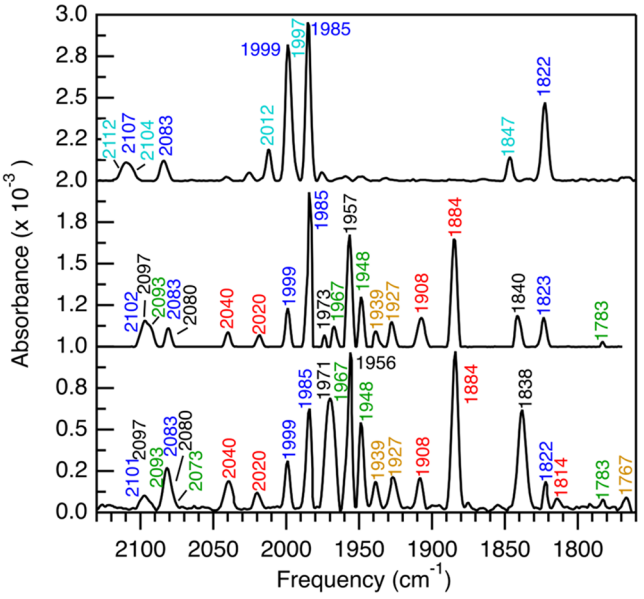

Figure 2. IR spectra of oxidized and H_2-treated CpIII. Top, spectrum of auto-oxidized (AO) CpIII (100 mg mL^{-1}) collected at 298 K. **Middle** and b**ottom**, AO sample treated under 1 atm of 100% H_2, pH 8, and collected at 195 K (**Middle**) or 10 K (**Bottom**). The signals are H_{ox+1}' (cyan), H_{ox+1} (blue), H_{ox} (green), H_{trans}-like (black), H_{red} (orange), and H_{redH+} (red).

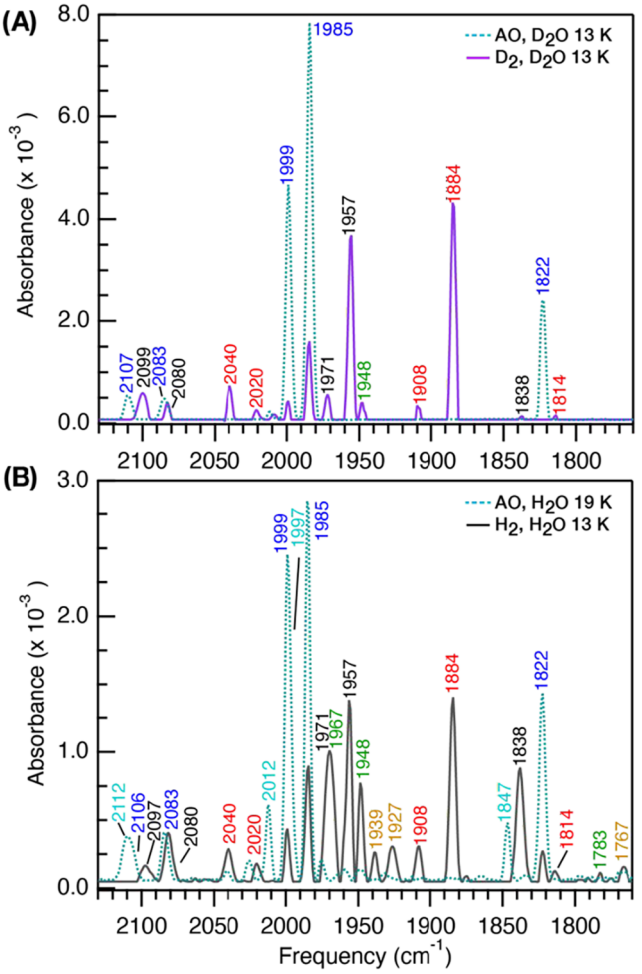

Figure 3. FTIR spectra of CpIII treated under 100% D_2 or 100% H_2. AO CpIII (100 mg mL^{-1}) was prepared in D_2O buffer, pD 8 (**A, aqua**), or H_2O buffer, pH 8 (**B, aqua**). Treatment on a Schlenk line under 1 atm of 100% D_2 (**A, purple; 4x intensity**) or 100% H_2 (**B, black**). H-cluster oxidation states; H_{ox+1} (blue), H_{ox+1}' (cyan), H_{ox} (green), H_{trans}-like (black), H_{red} (orange), and H_{redH+} (red). Spectra were collected at 298 or 13 K.

Schlenk line. AO CpIII C222S was prepared by storage of the as-isolated enzyme at 4 °C for a period of 11 days (Figures S7 and S8) or two months (Figure 5) without further reduction. Samples (15 μL) were loaded onto CaF_2 windows with 15 μm spacers, and spectra were collected in a custom-built, airtight sample holder.

EPR. AO CpIII and CpIII C222S were prepared as described above (Figures S3 and S8). CpIII treated with H_2, and sodium dithionite (Figures 4 and S3) was prepared by exchanging the AO enzyme into buffer containing 10 mM sodium dithionite and then subjected to headspace exchange into 100% H_2 as described above. Reduction with H_2 alone (Figure 4, middle) was performed by headspace exchange of AO CpIII with 100% H_2 using 10 vacuum/sparge cycles on a Schlenk line and incubated overnight at 4 °C prior to freezing. The CO-treated CpIII (Figure 4, bottom) was generated by first performing H_2 reduction, incubated overnight, and the following day an aliquot placed in a septum-sealed conical vial (N_2 headspace) and then sparged twice with 100% CO. 200 μL samples were loaded anaerobically into X-band EPR tubes of 3 mm ID (Wilmad lab glass, 707-SQ-250 mm). The preparation of CpIII redox titration samples (Figures S4–S6) included a cocktail of redox mediators as described.[6] All potentials are reported in mV vs NHE.

FTIR and EPR Spectra Collection and Processing. *FTIR.* Spectroscopy was performed at 298 K (spectra collected with an MCT detector) or at cryogenic temperatures (ColdEdge Technologies cryostat; spectra collected with a high-D* MCT detector) on an N_2-purged Nicolet 6700 Spectrometer (Thermo Fisher Scientific) as previously described.[53] Final spectra consist of 512 coadded scans at 2 cm^{-1} resolution. Baselines were manually corrected using sequential spline and linear functions, and in some cases water vapor background subtraction, in either the OMNIC software (Thermo Fisher Scientific) or IgorPro v9.

EPR. X-band (~9.38 GHz) CW EPR data were collected on an Elexsys E500 spectrometer equipped with a super high-Q resonator (Bruker), cryogen-free helium system (ColdEdge Technologies), and MercuryiTC temperature controller (Oxford Instruments, UK). Spectra were collected at various powers and temperatures (as indicated) by using a modulation frequency of 100 kHz and modulation amplitude of 10 G. EPR spectra were generally baseline corrected via subtraction of a polynomial function in IgorPro v9. For the full redox titration data set which is shown in reference 6 (data collected at T = 15 K with P = 1 mW) and used in conjunction with updated and new signal assignments to generate the current E_m analysis (Figure S4), the −29 mV spectrum was used to subtract a general buffer and redox-mediator background from all subsequent samples, with additional baseline correction performed as needed. We note this mediator background signal continued to grow at lower potentials and is accounted for in simulations of the 20 K data by the inclusion of an axial-type signal (see the Simulation of EPR Spectra section).

EPR Signal Identification. To obtain temperature-normalized spectra for analysis, variable-temperature CW spectra shown in Figures S3 and S5 were corrected for the

https://doi.org/10.1021/acs.biochem.5c00066
Biochemistry 2025, 64, 2455−2466

Species[a]	g-values[b]	E_m[8] (mV) (ox/red)[c]
H_{ox}	2.10, 2.02, 2.00	-407 (H_{ox+1}/H_{ox})
H_{trans}-like	2.07, 1.95, 1.87	-418 (H_{ox+1}/H_{trans}-like)
H_{red}, H_{redH+}	EPR silent	-455 to -485 (H_{ox}, H_{trans}-like/H_{red}, H_{redH+})
$FC1_{red}$	2.04, 1.94, 1.89	-404 ($FC1_{ox}/FC1_{red}$)
$FC2_{red}$	2.09, 1.93, 1.91	-406 ($FC2_{ox}/FC2_{red}$)

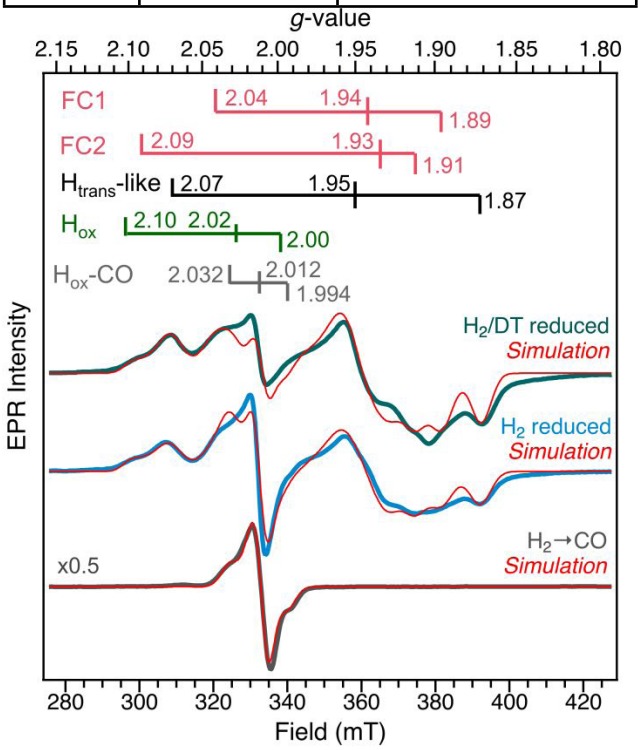

Figure 4. CW X-band EPR spectra of CpIII. AO CpIII was treated with either 1 atm of 100% H_2 in the presence of sodium dithionite (T = 20 K, P = 1 mW), **Top trace**; 100% H_2 and incubated overnight (T = 15 K, P = 1 mW), **Middle trace**; or 100% H_2 (overnight) followed by sparging under 100% CO (T = 15 K, P = 1 mW; data shown at half-intensity for visualization). Spectral simulations (**red traces**) comprised of H-cluster and F-cluster signals were performed using parameters in Table S2, and g-values are shown at the top.

Curie Law through multiplication of the spectra signal intensity by their respective collection temperatures. A power of 1 mW was commonly used, as qualitative analysis indicated minimal power saturation of any species when using this power to collect in their respective T_{opt} ranges.

H_{ox}-CO Signal. Initial attempts to simulate the CO-treated CpIII EPR signal (Figure 4) as a single rhombic-type species were not successful. The temperature-dependent behavior of the signal was then assessed which revealed differential temperature-dependent intensity changes for the central derivative feature compared to the wings of the spectrum. Further analysis provided evidence of a second unknown signal with distinct temperature-dependent behavior, which underlies the H_{ox}-CO signal. Simulation of the data using both the rhombic H_{ox}-CO signal (g = 2.0315, 2.012, and 1.9935) and a second signal (g = 2.017, 2.008, and 2.008) (Table S2) produced high-quality fits at all temperatures (see the Simulation of EPR Spectra section).

H_{ox} Signal. The H_{ox} signal of CpIII was first described in reference,[6] which used simulation of a potentiometric sample poised at −399 mV (T = 15 K; P = 1 mW) to determine a H_{ox} g-tensor of g = 2.10, 2.04, 1.99. As the first turning point of the H_{ox} signal (g_1 = 2.1) represents the low-field edge of the spectrum, it was used throughout as the primary feature to track H_{ox} in variable-temperature or potentiometric data. In this manner, the T_{opt} of the H_{ox} signal was determined from the H_2 reduced data to be in the range of 40−50 K (Figure S3; Table S2). This temperature response was confirmed with analysis of the −399 mV sample variable-temperature spectra (Figure S5), which also displayed a high population of H_{ox}. We also note the H_{ox} signal described in reference 6 is refined here as g = 2.10 2.024 1.998 (see the Simulation of EPR Spectra section).

H_{trans}-like Signal. The H_{trans}-like EPR signal was first identified from the H_2 reduced data (Figures 4 and S3) using additional features at $g \sim 2.07$ and $g \sim 1.87$ (modeled as the g_1 and g_3 values of a rhombic signal, respectively). Similar to the approach used to analyze H_{ox}, the H_{trans}-like feature at $g \sim 1.87$ was used primarily for analysis due to its position outside the other spectral features. Since signals from the F-clusters and H_{ox} considerably overlap the H_{trans}-like feature at $g \sim 2.07$, this feature was examined only as a comparison to aid in analysis. In this way, a T_{opt} of 20 K was determined for H_{trans}-like, with agreement from monitoring both features in the H_2 reduced data. Analysis of the H_{trans}-like signal in the −442 mV variable-temperature data set confirmed a T_{opt} = 20 K, with the features at g_1 and g_3 displaying T_{opt} ranges of 15−20 K and 20−30 K, respectively. The temperature range on analysis from −442 mV data is not surprising given the lower simulated population of H_{trans}-like signal in the −442 mV spectrum at 20 K compared with H_2 reduced (*vide infra*, Table S3).

F-Cluster Signals. Analysis of the spectra presented in this work allowed for further deconvolution of the F-cluster features (previously assigned)[6] into two discrete sets of signals, FC1 and FC2 (Table S2). These signals were most clearly resolved in the −399 mV spectra (Figures S5 and S6), particularly around their g_3 values (simulated as FC1 = 1.895; FC2 = 1.914). For more reduced samples (i.e., −442 mV, H_2-treated), the additional intensity was present in this region of the spectrum, as well as surrounding the g_2 of FC1 ($g \sim 2.04$), which hindered the resolution of the signals (Table S2, Figures S5−S6). Therefore, the temperature-dependent behavior of the F-cluster signals was analyzed using primarily the −399 mV spectra at the specific g_3 values given above. In these data, we note an apparent slight shift of the FC2 feature (g_3 = 1.914) to a higher g-value when going from 20 to 30 K (Figure S5). This could be due to additional spectral effects from spin−spin coupling between the FC1 and FC2 clusters, which generally resolve better with colder temperatures. This explanation is corroborated by analysis of the H_2 reduced and −442 mV spectra (Figures S3 and S5). While these signals display far less resolution in the spectral region due to the increased signal intensity, they indicate a similar temperature-dependent shift of the g_3 feature. Given these observations and the complexity of deconvoluting possible additional spin−spin coupling spectral effects, no difference was rigorously determined in the temperature-dependent behavior of the CpIII F-cluster signals obtained from these spectra, with a T_{opt} range of 20−30 K assigned for both FC1 and FC2 (Table S2). Likewise, we

https://doi.org/10.1021/acs.biochem.5c00066
Biochemistry 2025, 64, 2455−2466

were unable to resolve any significant difference in E_m values (Table 2; Figure S4) for the two cluster signals (*vide infra*).

Simulation of EPR Spectra. Simulations were performed using the EasySpin toolbox and its core function "pepper" within Matlab version R2020A (MathWorks) with full simulation parameters given in Table S2.[54] A gStrain parameter was used to replicate line broadenings. Spectra were not normalized prior to the simulation. Table S3 gives the relative populations of each EPR species, obtained from fitting the simulated intensity of each signal to the experimental spectral intensity, with the contribution of each species reported as a % of the total simulated intensity.

Using the T_{opt} values determined from analysis of temperature-normalized data (Table S2), a maximal intensity is obtained for the H_{trans}-like and FC signals between 20 and 30 K, and therefore data collected at 20 K were chosen for simulation to further deconvolute signal assignments and determine relative spectral contributions. Although the H_{ox} signal (T_{opt} = 40−50 K) experiences saturation effects at this temperature, the use of only 20 K data allows for a comparison of relative changes to the simulated H_{ox} contribution across the data set.

For simulation of the CO-treated data at 15 K (Figure 4) the H_{ox}-CO signal accounted for ∼ 75% of the total simulated spectrum with the underlying signal accounting for the remaining 25%. This ratio of 3:1 was similar to the ratio from the simulation of the H_2/sodium dithionite reduced spectrum collected at 20 K (Figure 4), however in this case we note the H_{ox}-CO and underlying signal combined account for only ∼2% of the total simulated spectral weight (Table S3). Simulations of redox titration data at 20 K (Figure S6) were performed with the inclusion of an axial-type radical signal with $g_\perp$ = 2.018 and $g_\parallel$ ∼ 2.01 (Table S2) to account for the contribution of redox mediators. This same background signal accounted for ∼2.4% (−399 mV), ∼1.8% (−442 mV), or ∼10% (−351 mV) of the total simulated intensity for the spectrum. We note the overall simulated signal intensity for the −351 mV spectrum is low compared to what is simulated for other samples (Table S3), which is unsurprising given the low overall signal intensity and resolution of H-cluster and F-cluster signals at this potential (Figure S5 and S6).

During these analyses, we also noted a clear difference in the quality of fit between the simulation of the less reduced (i.e., −399 mV) and the more reduced (i.e., −442 mV, H_2-treated) data. This was particularly true in the region of g ∼ 2.02, where multiple species overlap, and at g ∼ 1.9, where both FC1 and FC2 contribute. Spin−spin coupling between reduced FC1 and FC2 (*vide supra*) would contribute additional spectral complexity not accounted for by our simulations and would also be expected to impact the quality of the spectral fit more as reduction continues. We also note that the H_{ox} signal contribution in the middle of the spectrum (g_2 = 2.024) might impact the quality of the fit in this region due to the saturation effects, although the absence of any H_{ox} signals near g = 1.9 precludes this as the sole explanation for the additional experimental intensity.

The exact g-values used to simulate each spectrum are given in Table S2. Slight variations on the order of $\Delta g \leq 0.002$ were present in some of the g-values simulated in different samples. These shifts can generally be explained by the complexity of the spectral region due to overlapping species or other physical reasons, such as contributions from spin−spin coupling. As both F-clusters are reduced, spin−spin coupling between FC1 and FC2 can influence the line-shape and even position of the F-cluster spectral features. The exact measure of the spectral effect is dependent on the strength of coupling and the degree of reduction of both clusters, and effects can also be anisotropic (influencing parts of the spectrum differently) depending on the geometry of the magnetic interaction. As H_{ox} was simulated under conditions of temperature-saturation, a combination of fitting and global analysis that included higher temperature data was used to first refine the published g-tensor from Artz et al.[6] and the resulting g-values reported in Table S2 were used in subsequent simulations without additional fitting. The g_1 feature of the H_{trans}-like signal displayed the only shift (Δg = 0.0025) outside the range reported above, although this is in essence a difference between the H_2 reduced (g_1 = 2.072) and potentiometric (g_1 ∼ 2.07) data. These differences could result from the different methods of reduction and/or greater population of H_{trans}-like in the H_2 reduced sample. The derivative feature of the rhombic H_{trans}-like signal (i.e., g_2) was not fully resolved in any of the spectra analyzed here, however, comparison across data sets and reduction treatments showed that additional intensity was present at g ∼ 1.95 which correlated with the other H_{trans}-like features. The poor resolution of the feature made exact assignment difficult, and therefore, the g-value was first allowed to fit generally in this region. From these results, the value of g_2 = 1.952 (Table S2) was determined for use in subsequent simulations that reproduced the shape of the region relatively well (Figures 4 and S6).

Given the multiple, overlapping components in these data and the lack of additional constraints on fitting parameters to resolve the shifts described above, we report the final assigned signals of each species (except H_{ox}-CO) with g-values rounded to the nearest hundredth in the callouts at the top of Figures 4, S3, and S5−S6. The H_{ox}-CO signal was obtained from fitting of the data using only two components that resulted in high-quality simulations and is reported in the third decimal place. For simulation of the CpIII C222S variant in Figure S8 we include an additional resolution for g-values when simulated approximately halfway between the hundredth values.

E_m Analysis from 15 K EPR Titrations. Potentiometric titration of CpIII poised from −29 mV to −442 mV previously determined the CpIII H_{ox} signal to have an E_m[8] = −389 mV vs NHE.[6] A sample poised at −460 mV was also prepared and included in the E_m analysis of this work (Figure S4).

Potential-dependent changes in H-cluster or F-cluster signal intensities were monitored using the same features as those for temperature-dependent analyses (H_{ox}, g = 2.1; H_{trans}-like, g = 2.07; FC1, g = 1.895; FC2, g = 1.914). The n = 1 Nernstian behavior of the resultant data was then assessed by fitting the data to either eq 1 (FC1 and FC2) or eq 2 (H_{ox} and H_{trans}-like);

$$f(x) = y_0 + \frac{\text{maximum EPR signal}}{1 + e^{(x-E_m)F/RT}} \quad (1)$$

$$f(x) = y_0 + \frac{\text{maximum EPR signal}}{1 + e^{(x-E_m1)F/RT} + e^{(E_m2-x)F/RT}} \quad (2)$$

using a custom fit function in IgorPro v9 (y_0 = y-axis offset; x = potential in mV; E_m = midpoint potential in mV; F = Faraday constant = 96,480 C·mol^{-1}; R = Gas constant 8.314 J·K^{-1}·mol^{-1}; T = Temperature in K).[55] The 95% confidence band of each fit (where model points are expected to fall with a 95% or

https://doi.org/10.1021/acs.biochem.5c00066
Biochemistry 2025, 64, 2455−2466

greater probability) is included (Figure S4). The H-cluster signal of H_{ox} appeared not to reach a maximum intensity or level off before decreasing, indicating an equilibrium process due to steady-state conditions at the lowest potentials. Likewise, the H_{trans}-like signal displayed minimal intensity change at the end of the titration, although a significant decrease as observed for H_{ox} was not apparent, in line with a slightly lower E_m of formation for H_{trans}-like. Therefore, these data were fit to eq 2, which includes an expression for a second Nernstian process representing the H_{ox}, H_{trans}-like/H_{red}, and H_{redH+} couple. We note the lack of data constraining the fit of this second redox couple and present the results only to provide a general range.

Population Analyses from Spectral Simulations. The results of simulating select potentiometric data (Figure S6) are shown in Tables S2 and S3. Given the low signal quality in the −351 mV data, we refrain from ascribing too much significance to the simulated weights at this potential. Instead, we have included these data to illustrate the lack of any discernible H_{trans}-like contribution and provide context for the subsequent population increases simulated for all species.

Given its higher T_{opt}, it is likely the amount of H_{ox} is slightly underrepresented in the simulated weights (Table S3), however, examination of the 40 and 50 K data in the temperature-dependent data set of Figure S5 corroborate the trend of H_{ox} contribution from 20 K simulations. While the 20 K simulations show a similar simulated weight of H_{ox} for −399 and −442 mV samples (Table S3), the actual percent of the total simulated weight decreases from −399 to −442 mV as spectral intensity from other signals increases. The simulated weight of H_{ox} at −442 mV is also complicated by additional spectral intensity contributions from possible F-cluster spin−spin coupling at this potential. These results are in line with the E_m analysis, which indicates a decrease in the H_{ox} population at lower potentials that can be described with an $E_m \sim -455$ mV (Figure S4). Also, in agreement with the E_m analysis, the H_{trans}-like population determined from the simulated weights appears to increase as potential is lowered, in both absolute simulated intensity and as a percent contribution to the overall simulated intensity. The F-cluster trends are less straightforward, in a manner that matches the observed complexities and likely spectral contributions from spin−spin coupling.

RESULTS

IR Spectral Properties of Reduced CpIII. During a catalytic cycle, the H-cluster cycles through reduced and oxidized intermediates, which can be detected by Fourier transform infrared (FTIR, or IR) and electron paramagnetic resonance (EPR) spectroscopies. In IR spectroscopy, the reduction−oxidation of the H-cluster subsites can be detected as changes in νCO and νCN band frequencies. The IR and EPR spectra also can enable the resolution of isoelectronic states that differ in the distribution of electronic spin across the cluster, like H_{ox} and H_{trans}[56] or H_{hyd}[42,43,57,58] and H_{sredH+},[59−62] because the H-cluster EPR signals and diiron subsite νCO and νCN band frequencies are highly sensitive to the base electronic structure. IR is also powerful for detecting otherwise EPR silent, diamagnetic states, for example, the fully oxidized H-cluster[33] and the one-electron reduced H_{red} (defined here as $[4Fe\text{-}4S]^{+}$-$[Fe^{II}\text{-}Fe^{I}]$) or H_{redH+} (defined here as $[4Fe\text{-}4S]^{2+}$-$[Fe^{I}\text{-}Fe^{I}]$ states.[62−65]

To begin assigning the reduced H-cluster states of CpIII, the IR spectrum of the anaerobically oxidized (auto-oxidized, AO) was collected. The AO spectrum primarily consisted of the H_{ox+1} state, $[4Fe\text{-}4S]^{2+}$-$(Fe^{II}\text{-}Fe^{II})$,[6] composed of a distinct set of νCN bands at 2106 and 2083 cm^{-1}, νCO bands from terminally bound CO ligands (t-CO) at 1999, 1985, and the νCO band of a bridging CO ligand (μ-CO) at 1826 cm^{-1} (Figure 2 and Table 1). In some oxidized samples, a second set of νCO bands was observed at 2012, 1997, and 1850 cm^{-1}, which was assigned to a second H_{ox+1} state (Figures 2, 5, and S2) referred to here as H_{ox+1}' (Table 1).

Table 1. IR Signals of the CpIII H-Cluster Oxidation States

H-cluster	t-CN[a]	t-CO[a]	μ-CO[a]
H_{ox+1}'	2111, 2104	2012, 1997	1850
H_{ox+1}	2107, 2083	1999, 1985	1826
H_{ox}	2093, 2073	1967, 1948	1783
H_{trans}-like	2097, 2080	1971 1956	1838
H_{red}	2092, 2072	1939, 1927	1767
H_{redH+}	2040, 2020	1908, 1884	1814
$H_{ox\text{-}CO}$	2103, 2090	2009, 1978, 1959	1795

[a]Assignments for H_{ox+1} and H_{ox}, 298 K spectra in Figure 2; H_{trans}-like, H_{red}, H_{redH+}, 13 K spectra Figure 3; H_{ox}-CO, Figure S2.

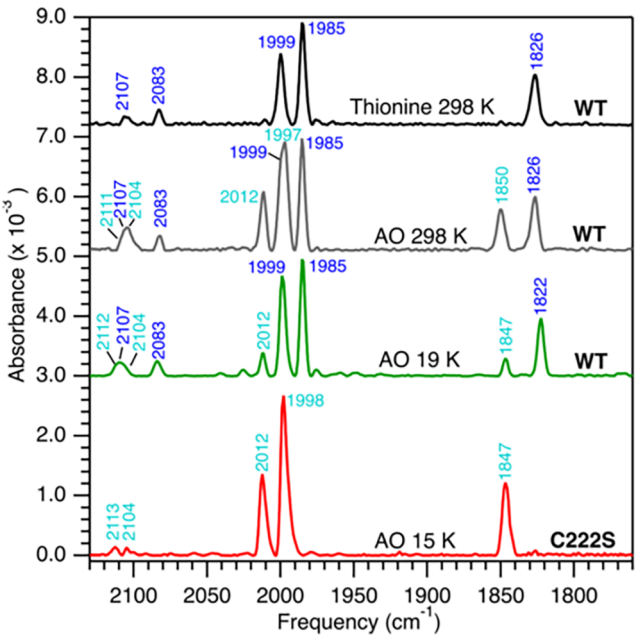

Figure 5. FTIR spectra of oxidized CpIII and CpIII C222S variants. Thionine oxidized CpIII collected at 298 K (**black**); AO collected at 298 K (**gray**) or 19 K (green); AO CpIII C222S collected at 13 K (**red**). The νCO and νCN modes of H-cluster states are labeled as H_{ox+1} (blue) and H_{ox+1}' (cyan). Samples were anaerobically purified in buffer with sodium dithionite (2 mM, pH 8), allowed to oxidize at 4 °C over a period of days, and exchanged into dithionite-free buffer prior to spectrum collection. WT = wild-type.

Equilibration of AO CpIII under 1 atm of H_2 resulted in significant changes in the νCO and νCN band frequencies, consistent with the reduction of the AO sample into a mixture of reduced states with different electronic structures (Figures 2 and S2). The use of cryogenic temperatures had two effects; (i) it reduced the rate of turnover, which led predominantly to the H_{ox+1} state in room temperature spectra, and (ii) led to less line broadening of the νCO bands for improved resolution of

https://doi.org/10.1021/acs.biochem.5c00066
Biochemistry 2025, 64, 2455−2466

spectral signals. It also revealed a temperature sensitivity of the μ-CO band frequencies of H_{ox+1} (Table S1), which we previously observed in [FeFe]-hydrogenase I of *Clostridium acetobutylicum* (CaI),[60] and has been observed by others.[66] For example, the comparison of spectra collected at 10 and 195 K led to resolution of spectral assignments to specific H-cluster oxidation states that were challenging to identify at 298 K (Figures 2, S2, and Table 1). In addition to H_{ox+1}, there were signals consistent with the H_{ox}, H_{red}, and H_{redH+} states that are observed in other [FeFe]-hydrogenases. There was no detectable IR signal, indicative of a fully reduced H_{sredH+} state.

In addition to the H-cluster states identified above, there was an additional signal with a set of terminal νCO bands at 1971, 1956, and a μ-CO band at 1838 cm^{-1} (black labels, Figure 2). These bands are similar to signals assigned to either the hydride-bound state, H_{hyd} ($[4Fe\text{-}4S]^{+}$-$[Fe^{II}\ Fe^{II}]$-H^{-}), or an H_{trans}-like state ($[4Fe\text{-}4S]^{+}$-$[Fe^{II}\ Fe^{II}]$), that have been observed in the Group A enzymes like CaI, CrHydA1 and DdH.[33,42,43,57,60] Although these two states share the same base redox level, the H_{hyd} state contains a terminally bound hydride that is distinguishable by a frequency shift in the μ-CO band under H/D isotope editing.[29,42,57,60] The shift is due to the *trans*-influence of a terminally bound hydride on the distal Fe atom (Fe_D), which modulates the Fe_D π-backbonding with the μ-CO. We used this property to test for H_{hyd} by monitoring the 1838 cm^{-1} μ-CO peak under H/D isotope enrichment, looking for an isotope-dependent shift that would indicate this signal is from the H_{hyd} (rather than H_{trans}) state.[42,67] Equilibration of CpIII in the H_{ox+1} state under 1 atm of H_2 (H_2O) or D_2 (D_2O) (Figure 3) led to mixtures of oxidized and reduced states, including the 1971, 1957, and 1838 cm^{-1} signal. Although the levels of H_{ox}, H_{red}, and H_{redH+} enrichment differed, and there are isotope effects on νCO peak intensities, there was no evidence for an H/D isotopic shift in the μ-CO band frequency. Taken together, the results support the assignment of the 1971, 1956, and 1838 cm^{-1} signals in the 10 K spectrum (the μ-CO band at 1838 cm^{-1} shifts to 1842 cm^{-1} at 195 K) to a H_{trans}-like state.

CO is known to react with [FeFe]-hydrogenases by binding to the H-cluster distal Fe site to form an oxidized CO-inhibited state, H_{ox}-CO. We tested the reactivity of CpIII to CO by incubating either the AO or H_2-treated CpIII with 100% CO and measuring the IR spectra. Whereas the AO sample was unreactive to CO (data not shown), when an H_2 reduced sample, composed of a mix of H_{ox+1}, H_{trans}-like, H_{ox} and H_{red} states, was incubated with CO it led to the conversion of the data to IR signal(s) consistent with the formation of H_{ox}-CO (Figure S2). Thus, in contrast to the H_{ox+1} state in the AO sample, the H_{ox+1} state present in the H_2 reduced sample reacts with CO.

EPR Analysis of the H_{ox}, H_{trans}-like States, and Reduced F-Clusters. To further aid in identifying the distribution and nature of the reduced intermediates, EPR spectra of reduced CpIII were collected. Samples reduced by H_2 either in the presence or absence of sodium dithionite (DT) showed approximately the same levels of the same signals (Figure 4, H_2/DT vs H_2) confirmed by simulation of the data (Tables S2 and S3). A slightly lower contribution from the H_{ox}-CO species (1.7 vs 6.7%, Table S3) was observed in the H_2/DT sample. Therefore, to simplify signal deconvolution, the EPR spectrum of H_2/DT reduced CpIII was further analyzed.

In accordance with the IR spectra of CpIII in Figures 2 and 3, simulation and analysis of the EPR spectra collected at different temperatures (Figures 4 and S3) identified discrete H-cluster signals. Temperature optima (T_{opt}) was used to make assignments of H_{ox}, an H_{trans}-like states. This also enables delineation of H_{trans},[56] and reduced FC1 and FC2 F-cluster signals, that have similar rhombic line-shape (Tables 2 and S1, S2). A small population of a signal with a more axial line-shape consistent with a CO-inhibited state (H_{ox}-CO) was also observed. This signal matched the signal at g = 2.032, 2.012, 1.994 of CpIII treated with H_2 followed by 100% CO (Figure 4 and Tables S1, S2). Additional intensity in the H_2 reduced data that was not accounted for by the simulation, particularly at $g \sim 1.9$, can be attributed to spin−spin coupling between reduced FC1 and FC2 clusters (see Materials and Methods). Spin−spin coupling between clusters, which has been observed for other [FeFe]-hydrogenases, is expected due to the short distance (11 Å) and side-chain packing between the F-clusters, as predicted from the AlphaFold model (Figure 1).[9,20,68] Consistent with the IR spectra results of reduced CpIII, there was no discernible H_{hyd} or H_{sredH+} like signal in these EPR spectra of reduced CpIII.

Table 2. CpIII H-Cluster and F-Cluster E_m Values[a]

species[a]	g-values[b]	E_m^8 (mV) (ox/red)[c]
H_{ox}	2.10, 2.02, 2.00	−407 (H_{ox+1}/H_{ox})
H_{trans}-like	2.07, 1.95, 1.87	−418 (H_{ox+1}/H_{trans}-like)
H_{red}, H_{redH+}	EPR silent	−455 to −485 (H_{ox}, H_{trans}-like/H_{red}, H_{redH+})
$FC1_{red}$	2.04, 1.94, 1.89	−404 ($FC1_{ox}$/$FC1_{red}$)
$FC2_{red}$	2.09, 1.93, 1.91	−406 ($FC2_{ox}$/$FC2_{red}$)

[a]The species in the titration. The specific identity of H_{ox+1} or H_{ox+1}' species was not determined and noted here as H_{ox+1}. [b]Values from simulation of EPR spectra (n = 1) in Figures 4 and S6. Full parameters are listed in Table S2. [c]The oxidized (ox) and reduced (red) species in the titration and their redox couple E_m values (mV vs NHE) at pH 8, obtained from the reanalysis of potentiometric EPR data reported in Artz et al.[6] to generate Nernst curves (Figure S4) for all the resolved EPR signals in Figures 4, S3, and S5.

The FTIR and EPR spectra of H_2 treated CpIII demonstrate that the H_{trans}-like state and H_{ox} are in equilibrium under reducing conditions. Based on the evidence of a H_{trans}-like state in CpIII, we re-evaluated the potentiometric EPR titration spectra reported in Artz et al.[6] using the EPR signals for the H_{trans}-like state and the FC1 and FC2 F-clusters resolved in this work (Figures S4−S6).

Fitting the intensity of the H_{trans}-like signal (monitored at g = 1.872 as a function of potential), to the n = 1 Nernst equation (eq S1) gave an estimated E_m^8 = −418 mV (Table 2). This transition is nearly isopotential with the E_m of H_{ox+1}/H_{ox}, which was refined here as E_m^8 = −407 mV. The E_m values for the F-cluster signals were determined to be E_m^8 = −404 mV for FC1 and E_m^8 = −406 mV for FC2 (Table 2). Further analysis and simulations of spectra, including additional variable-temperature EPR data collected on select potentiometric samples (Figure S5), revealed the H_{trans}-like state was stabilized to a higher level relative to H_{ox} in CpIII as potentials decreased to −442 mV (Figures S5 and S6), with a H_{trans}-like:H_{ox} ratio of 5:1 at −442 mV. This ratio increased when CpIII was equilibrated under H_2 to a value of 28:1 (Table S3). Poising CpIII at potentials below −450 mV led to a decline in the H_{ox} signal while the intensity of the H_{trans}-like signal appeared to

https://doi.org/10.1021/acs.biochem.5c00066
Biochemistry 2025, 64, 2455−2466

level out (Figure S4). Fits of each of the potentiometric plots to a second $n = 1$ Nernstian process (eq S2) gave an estimated E_m range of −455 to −485 mV for reduction of H_{ox}/H_{trans}-like states to H_{red}/H_{redH+} states. If the reduction of the H_{red}/H_{redH} state of the H-cluster of CpIII behaves in a Nernstian manner, then the E_m for the formation of H_{sredH+} would be expected to be less than −485 mV.

H_{ox+1} is Observed in a CpIII C222S Variant. As illustrated in Figures 1 and S1, the AlphaFold/AlphaFill structural model of CpIII predicts that each cysteine residue in the $TSC_{221}C_{222}C_{223}P$ motif has a specific function. C223 is predicted to be one of four cysteines that coordinate the $[4Fe\text{-}4S]_H$ subsite, C222 to function in proton transfer with the [2Fe] subsite, and C221 to be a supernumerary cysteine distal to the H-cluster. The proximity of the proton-transfer cysteine to the H-cluster not only enables proton exchange but, in unique cases, can promote a direct interaction of the Cys-SH group with the [2Fe] subsite. This interaction is observed in the X-ray crystallographic structure of aerobically prepared [FeFe]-hydrogenase CbA5H of *C. beijerinckii*.[36] Aerobically prepared CbA5H also stabilizes an inactive state, H_{inact}, that is EPR silent and has a similar IR signal to the H_{ox+1} and H_{ox+1}' states of CpIII (Tables 1 and S3).[16,31,36] Exchange of the conserved cysteine to either aspartic acid or alanine resulted in the loss of the ability to form the H_{inact} state and resistance to oxygen.[36]

We tested whether stabilization of H_{ox+1} in CpIII might be through a similar interaction of cysteine-SH with Fe_D by exchanging the predicted proton transfer cysteine, C222, to S222. A structurally conserved change that replaces the -SH group with an -OH group. The purified CpIII C222S variant had an H_2 evolution activity of 30 μmol H_2 min^{-1} mg^{-1}, which was 10-fold lower than the reported 305 μmol H_2 min^{-1} mg^{-1} of CpIII.[6] FTIR of the AO CpIII $C_{222}S$ variant collected at 298 K (Figure S7) or 15 K (Figure 5) showed that the Cys-to-Ser change did not result in a loss of the H_{ox+1} states. Compared to AO CpIII, the FTIR spectrum of the AO CpIII C222S had a higher enrichment of the H_{ox+1}' state versus H_{ox+1}. There were slight temperature-dependent shifts in the μ-CO band of H_{ox+1}' at 1847 (1850) and H_{ox+1} at 1822 (1826) cm^{-1} (Figures 5 and S7; frequencies from the 298 K spectrum of native CpIII are in parentheses). In addition, there were small contributions from H_{ox} and H_{trans}-like H-cluster states observed in the 298 K spectrum (Figure S7). The corresponding EPR spectrum (Figure S8) showed the majority of reduced FC1 and FC2 signals with contribution from a similar composition of H-cluster states, consisting of H_{ox} and H_{trans}-like signals (Figure S8, Tables S2 and S3).

DISCUSSION

Earlier EPR and IR experiments on CpIII had demonstrated that H_{ox+1} was stabilized at potentials below −418 mV based on the absence of H_{ox}, which did not account for the possibility of a H_{trans} state as an intermediate. Here using EPR and IR to analyze reduced CpIII we were able to demonstrate that reduction of H_{ox+1} not only forms H_{ox} but also leads to an H_{trans}-like state with an E_m^8 = −418 mV. Although the E_m^8 value is similar to H_{ox} (E_m^8 = −407 mV), at these potentials, the H_{trans}-like state is more populated than H_{ox} (by as much as 28:1).[32,33] By comparison, the H_{trans} state in DdH has a much more positive E_m than that of H_{ox}, where H_{ox} is the dominant species at potentials near the value of the H^+/H_2 couple (E_m = −472 mV, pH 8, 1 atm H_2).[33] The stability of an H_{trans}-like state in CpIII at a much lower potential of ∼ −418 mV implicates but does not prove that it may have a possible role in catalysis.

The most reduced H-cluster states in CpIII observed under the conditions of this study were H_{red} and H_{redH+} with an E_m range of −455 to −485 mV based on the modeled decay of H_{trans}-like and H_{ox} EPR signals (Figure S4). Strikingly, there was no detectable EPR or IR signal of either a super-reduced, H_{sredH+} state, or a hydride-bound state, H_{hyd}. While the lack of these states in this study does not necessarily rule out their occurrence, the distribution of reduced states thus far observed for CpIII is unlike most of the Group A, C, and D [FeFe]-hydrogenases. A comparison of the H-cluster intermediates of CpIII from these findings and comparison to those established for the Group A, C, and D enzymes is summarized in Table 3.

Table 3. Summary of the CpIII H-Cluster Redox States Compared to Group A, C, and D Enzymes

state	group A, C, D	CpIII (Group B)
oxidized[a]	H_{inact}, $[2^+]$-[II/II]	H_{ox+1}, $[2^+]$-[II/II]
	State 1, $[2^+]$-[II/II]	H_{ox+1}', $[2^+]$-[II/II]
	State 2, $[2^+]$-[II/I]	H_{ox}, $[2^+]$-[II/I]
	H_{air}-ox $[2^+]$-[II/I]	
	H_{ox}, $[2^+]$-[II/I]	
	H_{trans}, $[1^+]$-[II/II]	H_{trans}-like, $[1^+]$-[II/II]
1 e^- reduced	H_{red}, $[1^+]$-[II/I]	H_{red}, $[1^+]$-[II/I]
	H_{redH+}, $[2^+]$-[I/I]	H_{redH+}, $[2^+]$-[I/I]
2 e^- reduced	H_{sredH+}, $[1^+]$-[I/I]	not detected
	H_{hyd}, $[1^+]$-[II/II]-H^-	

[a]"Oxidized" here refers to species identified as inhibited or resting states, which for Group A, C, D enzymes includes H_{inact}, H_{air}-ox, H_{ox}, and state 1 and state 2.[16,17,31,32,34]

The unique oxidation states of CpIII that have been established here coincide with several variations in H-cluster coordination sphere residues compared to those of Group A enzymes (Figure 1). This suggests a functional role for the coordination sphere in controlling the catalytic properties of the H-cluster. As shown in the AlphaFold/AlphaFill model of CpIII in Figure 1, there are specific structural differences in CpIII that include an F/G pair near the μ-CO of the [2Fe] subsite that replaces the T/M pair in CpI, where the methionine side chain is replaced by a more hydrophobic benzyl group of phenylalanine. Similar variations in these amino acid positions, either F/G or F/S, are observed in *Thermotoga maritima* HydS Group C bifurcating and *Tam*HydS Group D H_2-sensing [FeFe]-hydrogenases, respectively.[15,69] These enzymes exhibit decreased H_2 evolution activities compared to Group A [FeFe]-hydrogenases as well as increased resistance to CO inhibition. *Tam*HydS variants that have changes in proton-transfer pathway residues stabilize an EPR silent State 1 that has an IR spectrum similar to H_{ox+1}.[34] CpIII and *Tam*HydS share similar μ-CO environments, suggesting there may be a connection between the local H-cluster environment and the ability to stabilize fully oxidized H-cluster states. Another example is the role of a methionine near the μ−CO in Group A enzymes that exist in different structural conformations. This flexibility is also observed as a change in the orientation of the Met side chain to μ-CO upon CO ligand binding at Fe_D.[6,70] Altogether, the composition and interaction of amino acids (i.e., Phe or Met) near the μ-CO ligand appear to be a mechanism by which [FeFe]-hydro-

https://doi.org/10.1021/acs.biochem.5c00066
Biochemistry 2025, 64, 2455−2466

genases modulate the stabilization of H-cluster intermediates and catalytic reactivity.

Another unique feature of CpIII is the presence of a supernumerary cysteine, or C221, that is located within the TSCCCP motif and absent in Group A, C and D enzymes.[71−73] A recent study tested the role of an extra cysteine in the reactivity of CpIII using electrochemical kinetics.[19] The results demonstrated that two independent, inactive species, I_1 and I_2 were formed at high (E^0 = −139 mV) and low (E^0 = −384 mV) potentials, respectively. Based on the similarity of the E^0 value of I_2 to the E_m[8] = −389 mV of the CpIII H_{ox+1},[6] the authors proposed that I_2 and H_{ox+1} were the same H-cluster state. A deletion of C223, predicted to coordinate the [4Fe-4S] subsite (Figure 1) was used to convert the CpIII TSCCCP motif into a canonical TSCCP motif and resulted in a variant that lost 97% of the native CpIII activity as well as the ability to form the low potential, I_2, state.[19] Based on these results, the authors proposed that C222 in native CpIII, which is assigned as the proton-transfer cysteine, forms an essential cysteine−SH interaction at Fe_D similar as observed in CbA5H. This interaction was determined to stabilize the I_2 state leading to the conclusion that I_2 (and therefore, the previously reported H_{ox+1} state)[6] is H_{inact}.

In this work, we established that there are several properties of CpIII H_{ox+1} that differentiate it from H_{inact} of CbA5H and DdH, which has been shown to be a result of SH interaction with the [2Fe] subsite, either in the form of sulfide binding or cysteine coordination. First, we reassigned the E_m (pH 8) value of H_{ox+1} to either −407 mV for H_{ox+1}/H_{ox}, or −418 mV for H_{ox+1}/H_{trans} (Table 2). These values are more negative than the −357 mV (pH 7.4) value of the H_{ox}/H_{inact} couple in CbA5H or −92 mV (pH 8) value for the H_{inact}/H_{trans} couple in DdH.[33] Second, unlike the H_{inact} states of CbA5H and DdH, the H_{ox+1} states of CpIII are observed in anaerobically prepared samples, or after reaction of resting H_{ox+1} with H_2 (see Figures 2, 3, and S2). These conditions do not include extraneous sulfide,[2,30,32,36,38] and our use of a biosynthetic maturation process to prepare CpIII alleviates H-cluster damage that can occur with chemically prepared diiron compounds.[6,13,21,25,26,31,41−48,57,60] Apparently if the process has a low efficiency and incubation time, it can result in damage of the diiron compound and release of CN(−) (and CO) leading to the formation of H_{inact}-like, and H_{trans}-like(CN-) bound states.[40] Third, in CbA5H, the formation of H_{inact} requires the proton-transfer cysteine and was lost when exchanged to either aspartate or alanine,[36] whereas, in CpIII the H_{ox+1} states are observed when this cysteine is exchanged to serine (Figure 5). Altogether, these details reveal distinguishing properties of the CpIII H_{ox+1} state that point to possible functional differences compared to H_{inact} of CbA5H and DdH[36,39] but with possible similarity to the function of State 1 of *Tam*HydS.[34] For the latter, possible aquo or hydroxide coordination at the [2Fe] subsite has been proposed,[34] and while this may also be possible for CpIII, a detailed structural determination will be required to resolve the exact nature of the H_{ox+1} state.

CONCLUSIONS

Overall, our studies on CpIII expand on the growing evidence that plasticity in the amino acids that form the secondary coordination sphere of the H-cluster functions to control oxidation states and catalysis. Future studies will address how the oxidation states of the H-cluster in CpIII culminate in the mechanism of H_2 activation and catalysis. Resolving how the structural variations in CpIII support variation in H-cluster states and catalysis will add to the emerging understanding of how natural variation in cofactor sites, proton transfer residues, and conformational flexibility[2,6,15,17,34,39] create profound differences in the catalytic properties and reactivity of hydrogenases to fulfill the diverse functions of these enzymes in metabolism.

ASSOCIATED CONTENT

Supporting Information

The Supporting Information is available free of charge at https://pubs.acs.org/doi/10.1021/acs.biochem.5c00066.

Figure S1, Comparison of the AlphaFold/AlphaFill structural model and H-cluster environment of CpIII with the structure of CpI; Figure S2, FTIR spectra of CpIII treated with H_2 and CO; Figure S3, variable-temperature spectra collected on H_2-treated CpIII; Figure S4, plot of the midpoint potential analysis of potentiometric EPR spectra; Figure S5, variable-temperature EPR spectra collected on redox titration samples of CpIII; Figure S6, EPR simulations of potentiometric data collected at 20 K; Figure S7, FTIR spectra of AO native CpIII and CpIII C222S; Figure S8, EPR spectrum and simulation of auto-oxidized CpIII C222S. Table S1, FTIR signal assignments of CpIII and other [FeFe]-hydrogenases; Table S2, temperature and simulation parameters from EPR spectra of CpIII; Table S3, population analysis from simulation of EPR data (PDF)

CpIII AlphaFold/AlphaFill structural model manually refined to include the H-cluster and two F-clusters (PDB)

AUTHOR INFORMATION

Corresponding Authors

David W. Mulder − *Biosciences Center, National Renewable Energy Laboratory, Golden, Colorado 80401, United States;* orcid.org/0000-0003-0559-0145; Email: david.mulder@nrel.gov

Paul W. King − *Biosciences Center, National Renewable Energy Laboratory, Golden, Colorado 80401, United States; Renewable and Sustainable Energy Institute (RASEI), University of Colorado Boulder, Boulder, Colorado 80303, United States;* orcid.org/0000-0001-5039-654X; Email: paul.king@nrel.gov

Authors

Effie C. Kisgeropoulos − *Biosciences Center, National Renewable Energy Laboratory, Golden, Colorado 80401, United States;* orcid.org/0000-0003-1842-5691

Michael W. Ratzloff − *Biosciences Center, National Renewable Energy Laboratory, Golden, Colorado 80401, United States*

Ekaterina M. Stroeva-Dahl − *Biosciences Center, National Renewable Energy Laboratory, Golden, Colorado 80401, United States*

Sarah Hasan − *Biosciences Center, National Renewable Energy Laboratory, Golden, Colorado 80401, United States;* orcid.org/0000-0003-4125-0025

Febin Varghese − *Institute of Biological Chemistry, Washington State University, Pullman, Washington 99163, United States*

https://doi.org/10.1021/acs.biochem.5c00066
Biochemistry 2025, 64, 2455−2466

Jacob H. Artz − *Biosciences Center, National Renewable Energy Laboratory, Golden, Colorado 80401, United States*
John W. Peters − *Department of Chemistry and Biochemistry, University of Oklahoma, Norman, Oklahoma 73019, United States;* orcid.org/0000-0001-9117-9568

Complete contact information is available at: https://pubs.acs.org/10.1021/acs.biochem.5c00066

Author Contributions

[⊥]E.C.K., M.W.R., S.H., and J.H.A. contributed equally to this work. The manuscript was written through contributions of all authors. All authors have given approval to the final version of the manuscript.

Funding

U.S. Department of Energy Office of Basic Energy Sciences, Division of Chemical Sciences, Geosciences, and Biosciences, Photosynthetic Systems Program. National Institutes of Health, National Institute of General Medical Sciences.

Notes

The authors declare no competing financial interest.

■ ACKNOWLEDGMENTS

Funding for this work was provided by the U.S. Department of Energy Office of Basic Energy Sciences, Division of Chemical Sciences, Geosciences, and Biosciences, Photosynthetic Systems Programs (E.C.K., M.W.R., E.M.S-D., J.H.A, D.W.M. P.W.K.). J.W.P. was supported by the National Institutes of Health (1R01GM138592-01). This work was authored in part by the Alliance for Sustainable Energy, LLC, the manager, and operator of the National Renewable Energy Laboratory for the U.S. Department of Energy (DOE) under Contract No. DEAC36-08GO28308. S.H. was supported by the U.S. Department of Energy, Office of Science, Office of Workforce Development for Teachers and Scientists (WDTS) under the Science Undergraduate Laboratory Internship (SULI) program. The U.S. Government and the publisher, by accepting the article for publication, acknowledge that the U.S. Government retains a nonexclusive, paid-up, irrevocable, worldwide license to publish or reproduce the published form of this work, or allow others to do so, for U.S. Government purposes.

■ ABBREVIATIONS

CpI, *Clostridium pasteurianum* [FeFe]-hydrogenase I; CpII, *Clostridium pasteurianum* [FeFe]-hydrogenase II; CpIII, *Clostridium pasteurianum* [FeFe]-hydrogenase III; DdH, *Desulfovibrio desulfuricans* [FeFe]-hydrogenase; CbA5H, *Clostridium beijerinckii* [FeFe]-hydrogenase; H-cluster, the [FeFe]-hydrogenase catalytic site cofactor; F-cluster, accessory iron−sulfur cluster; FC1, F-cluster 1; FC2, F-cluster 2; AO, auto-oxidized; H_{inact}, fully oxidized, inactive H-cluster; H_{ox+1}, H_{ox+1}', fully oxidized H-cluster; H_{ox}, one-electron reduced H-cluster, $[4Fe\text{-}4S]^{2+}$-$[Fe^{I}{-}Fe^{II}]$; H_{trans}, and H_{trans}-like, the one-electron reduced H-cluster; $[4Fe\text{-}4S]^{+}$-$[Fe^{II}{-}Fe^{II}]$; H_{red}, one-electron reduced H-cluster; $[4Fe\text{-}4S]^{+}$-$[Fe^{II}{-}Fe^{I}]$; H_{redH+}, one-electron reduced H-cluster, $[4Fe\text{-}4S]^{2+}$-$[Fe^{I}{-}Fe^{I}]$; H_{hyd}, one-electron reduced H-cluster with a hydride, $[4Fe\text{-}4S]^{+}$-$[Fe^{II}{-}Fe^{II}]$-H^{-}; H_{sred}, super-reduced, or 2-electron reduced H-cluster, $[4Fe\text{-}4S]^{+}$-$[Fe^{I}{-}Fe^{I}]$; H_{ox}-CO, CO-inhibited state; CpIII C222S, CpIII with a serine-to-cysteine change at amino acid C222; FTIR, Fourier transform infrared spectroscopy; EPR, electron paramagnetic resonance spectroscopy; CO, carbon monoxide ligand; CN, cyanide ligand; Fe_D, distal Fe atom of the H-cluster diiron subsite; NaDT, sodium dithionite; T_{opt}, optimal temperature; mW, milliwatt

■ REFERENCES

(1) Benoit, S. L.; Maier, R. J.; Sawers, R. G.; Greening, C. Molecular Hydrogen Metabolism: a Widespread Trait of Pathogenic Bacteria and Protists. *Microbiol. Mol. Biol. Rev.* **2020**, *84* (1), No. e00092-19, DOI: 10.1128/MMBR.00092-19.
(2) Morra, S. Fantastic [FeFe]-Hydrogenases and Where to Find Them. *Front. Microbiol.* **2022**, *13*, No. 853626, DOI: 10.3389/fmicb.2022.853626.
(3) Nicolet, Y.; Piras, C.; Legrand, P.; Hatchikian, C. E.; Fontecilla-Camps, J. C. *Desulfovibrio desulfuricans* iron hydrogenase: the structure shows unusual coordination to an active site Fe binuclear center. *Structure* **1999**, *7* (1), 13−23.
(4) Peters, J. W.; Lanzilotta, W. N.; Lemon, B. J.; Seefeldt, L. C. X-ray Crystal Structure of the Fe-Only Hydrogenase (CpI) from *Clostridium pasteurianum* to 1.8 Angstrom Resolution. *Science* **1998**, *282* (5395), 1853−1858.
(5) Fan, H.-J.; Hall, M. B. A Capable Bridging Ligand for Fe-Only Hydrogenase: Density Functional Calculations of a Low-Energy Route for Heterolytic Cleavage and Formation of Dihydrogen. *J. Am. Chem. Soc.* **2001**, *123* (16), 3828−3829.
(6) Artz, J. H.; Zadvornyy, O. A.; Mulder, D. W.; Keable, S. M.; Cohen, A. E.; Ratzloff, M. W.; Williams, S. G.; Ginovska, B.; Kumar, N.; Song, J.; McPhillips, S. E.; Davidson, C. M.; Lyubimov, A. Y.; Pence, N.; Schut, G. J.; Jones, A. K.; Soltis, S. M.; Adams, M. W. W.; Raugei, S.; King, P. W.; Peters, J. W. Tuning Catalytic Bias of Hydrogen Gas Producing Hydrogenases. *J. Am. Chem. Soc.* **2020**, *142* (3), 1227−1235.
(7) Poudel, S.; Tokmina-Lukaszewska, M.; Colman, D. R.; Refai, M.; Schut, G. J.; King, P. W.; Maness, P.-C.; Adams, M. W. W.; Peters, J. W.; Bothner, B.; Boyd, E. S. Unification of [FeFe]-hydrogenases into three structural and functional groups. *Biochim. Biophys. Acta, Gen. Subj.* **2016**, *1860* (9), 1910−1921.
(8) Caserta, G.; Papini, C.; Adamska-Venkatesh, A.; Pecqueur, L.; Sommer, C.; Reijerse, E.; Lubitz, W.; Gauquelin, C.; Meynial-Salles, I.; Pramanik, D.; Artero, V.; Atta, M.; del Barrio, M.; Faivre, B.; Fourmond, V.; Léger, C.; Fontecave, M. Engineering an [FeFe]-Hydrogenase: Do Accessory Clusters Influence O2 Resistance and Catalytic Bias? *J. Am. Chem. Soc.* **2018**, *140* (16), 5516−5526.
(9) Rodríguez-Maciá, P.; Pawlak, K.; Rüdiger, O.; Reijerse, E. J.; Lubitz, W.; Birrell, J. A. Intercluster Redox Coupling Influences Protonation at the H-cluster in [FeFe] Hydrogenases. *J. Am. Chem. Soc.* **2017**, *139* (42), 15122−15134.
(10) Adams, M. W.; Eccleston, E.; Howard, J. B. Iron-sulfur clusters of hydrogenase I and hydrogenase II of Clostridium pasteurianum. *Proc. Natl. Acad. Sci. U. S. A.* **1989**, *86* (13), 4932−4936.
(11) Fasano, A.; Fourmond, V.; Léger, C. Outer-sphere effects on the O2 sensitivity, catalytic bias and catalytic reversibility of hydrogenases. *Chemical Science* **2024**, *15* (15), 5418−5433.
(12) Gauquelin, C.; Baffert, C.; Richaud, P.; Kamionka, E.; Etienne, E.; Guieysse, D.; Girbal, L.; Fourmond, V.; André, I.; Guigliarelli, B. Roles of the F-domain in [FeFe] hydrogenase. *Biochim. Biophys. Acta, Bioenerg.* **2018**, *1859* (2), 69−77.
(13) Kisgeropoulos, E. C.; Artz, J. H.; Blahut, M.; Peters, J. W.; King, P. W.; Mulder, D. W. Properties of the iron-sulfur cluster electron transfer relay in an [FeFe]-hydrogenase that is tuned for H2 oxidation catalysis. *J. Biol. Chem.* **2024**, *300* (6), No. 107292, DOI: 10.1016/j.jbc.2024.107292.
(14) Greening, C.; Biswas, A.; Carere, C. R.; Jackson, C. J.; Taylor, M. C.; Stott, M. B.; Cook, G. M.; Morales, S. E. Genomic and metagenomic surveys of hydrogenase distribution indicate H2 is a widely utilised energy source for microbial growth and survival. *ISME J.* **2016**, *10* (3), 761−777.
(15) Chongdar, N.; Birrell, J. A.; Pawlak, K.; Sommer, C.; Reijerse, E. J.; Rüdiger, O.; Lubitz, W.; Ogata, H. Unique Spectroscopic

Properties of the H-Cluster in a Putative Sensory [FeFe] Hydrogenase. *J. Am. Chem. Soc.* **2018**, *140* (3), 1057−1068.
(16) Corrigan, P. S.; Majer, S. H.; Silakov, A. Evidence of Atypical Structural Flexibility of the Active Site Surrounding of an [FeFe] Hydrogenase from Clostridium beijerinkii. *J. Am. Chem. Soc.* **2023**, *145* (20), 11033−11044.
(17) Land, H.; Sekretareva, A.; Huang, P.; Redman, H. J.; Németh, B.; Polidori, N.; Mészáros, L. S.; Senger, M.; Stripp, S. T.; Berggren, G. Characterization of a putative sensory [FeFe]-hydrogenase provides new insight into the role of the active site architecture. *Chem. Sci.* **2020**, *11* (47), 12789−12801.
(18) Rodríguez-Maciá, P.; Kertess, L.; Burnik, J.; Birrell, J. A.; Hofmann, E.; Lubitz, W.; Happe, T.; Rüdiger, O. His-Ligation to the [4Fe−4S] Subcluster Tunes the Catalytic Bias of [FeFe] Hydrogenase. *J. Am. Chem. Soc.* **2019**, *141* (1), 472−481.
(19) Fasano, A.; Jacq-Bailly, A.; Wozniak, J.; Fourmond, V.; Léger, C. Catalytic Bias and Redox-Driven Inactivation of the Group B FeFe Hydrogenase CpIII. *ACS Catal.* **2024**, *14* (9), 7001−7010.
(20) Kisgeropoulos, E. C.; Bharadwaj, V. S.; Mulder, D. W.; King, P. W. The Contribution of Proton-Donor pKa on Reactivity Profiles of [FeFe]-hydrogenases. *Front. Microbiol.* **2022**, *13*, No. 903951, DOI: 10.3389/fmicb.2022.903951.
(21) Artz, J. H.; Mulder, D. W.; Poudel, S.; Colman, D.; Schut, G. J.; Williams, S. G.; Jones, A. K.; Adams, M. W. W.; Boyd, E. S.; King, P. W.; Peters, J. W. Structure-function of [FeFe]- and [NiFe]-Hydrogenases: an Overview of Diversity, Mechanism, Maturation, and Bifurcation. In *Microalgal Hydrogen Production: Achievements and Perspectives*; Seibert, M.; Torzillo, G., Eds.; The Royal Society of Chemistry, 2018; pp 31−66.
(22) Calusinska, M.; Happe, T.; Joris, B.; Wilmotte, A. The surprising diversity of clostridial hydrogenases: a comparative genomic perspective. *Microbiology (Reading)* **2010**, *156* (Pt 6), 1575−1588.
(23) Greening, C.; Cabotaje, P. R.; Valentin Alvarado, L. E.; Leung, P. M.; Land, H.; Rodrigues-Oliveira, T.; Ponce-Toledo, R. I.; Senger, M.; Klamke, M. A.; Milton, M.; Lappan, R.; Mullen, S.; West-Roberts, J.; Mao, J.; Song, J.; Schoelmerich, M.; Stairs, C. W.; Schleper, C.; Grinter, R.; Spang, A.; Banfield, J. F.; Berggren, G. Minimal and hybrid hydrogenases are active from archaea. *Cell* **2024**, *187* (13), 3357−3372.e19.
(24) Meyer, J. [FeFe] hydrogenases and their evolution: a genomic perspective. *Cell. Mol. Life Sci.* **2007**, *64* (9), No. 1063.
(25) Mulder, D. W.; Shepard, E. M.; Meuser, J. E.; Joshi, N.; King, P. W.; Posewitz, M. C.; Broderick, J. B.; Peters, J. W. Insights into [FeFe]-Hydrogenase Structure, Mechanism, and Maturation. *Structure* **2011**, *19* (8), 1038−1052.
(26) Peters, J. W.; Schut, G. J.; Boyd, E. S.; Mulder, D. W.; Shepard, E. M.; Broderick, J. B.; King, P. W.; Adams, M. W. [FeFe]-and [NiFe]-hydrogenase diversity, mechanism, and maturation. *Biochim. Biophys. Acta, Mol. Cell Res.* **2015**, *1853* (6), 1350−1369.
(27) Cornish, A. J.; Gärtner, K.; Yang, H.; Peters, J. W.; Hegg, E. L. Mechanism of Proton Transfer in [FeFe]-Hydrogenase from Clostridium pasteurianum*. *J. Biol. Chem.* **2011**, *286* (44), 38341−38347.
(28) Duan, J.; Senger, M.; Esselborn, J.; Engelbrecht, V.; Wittkamp, F.; Apfel, U.-P.; Hofmann, E.; Stripp, S. T.; Happe, T.; Winkler, M. Crystallographic and spectroscopic assignment of the proton transfer pathway in [FeFe]-hydrogenases. *Nat. Commun.* **2018**, *9* (1), No. 4726.
(29) Pham, C. C.; Mulder, D. W.; Pelmenschikov, V.; King, P. W.; Ratzloff, M. W.; Wang, H.; Mishra, N.; Alp, E. E.; Zhao, J.; Hu, M. Y.; Tamasaku, K.; Yoda, Y.; Cramer, S. P. Terminal Hydride Species in [FeFe]-Hydrogenases Are Vibrationally Coupled to the Active Site Environment. *Angew. Chem., Int. Ed.* **2018**, *57* (33), 10605−10609.
(30) Corrigan, P. S.; Tirsch, J. L.; Silakov, A. Investigation of the Unusual Ability of the [FeFe] Hydrogenase from *Clostridium beijerinckii* to Access an O2-Protected State. *J. Am. Chem. Soc.* **2020**, *142* (28), 12409−12419.
(31) Morra, S.; Arizzi, M.; Valetti, F.; Gilardi, G. Oxygen Stability in the New [FeFe]-Hydrogenase from *Clostridium beijerinckii* SM10 (CbA5H). *Biochemistry* **2016**, *55* (42), 5897−5900.
(32) Rodríguez-Maciá, P.; Reijerse, E. J.; van Gastel, M.; DeBeer, S.; Lubitz, W.; Rüdiger, O.; Birrell, J. A. Sulfide Protects [FeFe] Hydrogenases From O2. *J. Am. Chem. Soc.* **2018**, *140* (30), 9346−9350.
(33) Roseboom, W.; De Lacey, A. L.; Fernandez, V. M.; Hatchikian, E. C.; Albracht, S. P. J. The active site of the [FeFe]-hydrogenase from *Desulfovibrio desulfuricans*. II. Redox properties, light sensitivity and CO-ligand exchange as observed by infrared spectroscopy. *JBIC, J. Biol. Inorg. Chem.* **2006**, *11* (1), 102−118.
(34) Cabotaje, P. R.; Walter, K.; Zamader, A.; Huang, P.; Ho, F.; Land, H.; Senger, M.; Berggren, G. Probing Substrate Transport Effects on Enzymatic Hydrogen Catalysis: An Alternative Proton Transfer Pathway in Putatively Sensory [FeFe] Hydrogenase. *ACS Catal.* **2023**, *13* (15), 10435−10446.
(35) Felbek, C.; Arrigoni, F.; de Sancho, D.; Jacq-Bailly, A.; Best, R. B.; Fourmond, V.; Bertini, L.; Léger, C. Mechanism of Hydrogen Sulfide-Dependent Inhibition of FeFe Hydrogenase. *ACS Catal.* **2021**, *11* (24), 15162−15176.
(36) Winkler, M.; Duan, J.; Rutz, A.; Felbek, C.; Scholtysek, L.; Lampret, O.; Jaenecke, J.; Apfel, U.-P.; Gilardi, G.; Valetti, F.; Fourmond, V.; Hofmann, E.; Léger, C.; Happe, T. A safety cap protects hydrogenase from oxygen attack. *Nat. Commun.* **2021**, *12* (1), No. 756.
(37) Martini, M. A.; Rüdiger, O.; Breuer, N.; Nöring, B.; DeBeer, S.; Rodríguez-Maciá, P.; Birrell, J. A. The Nonphysiological Reductant Sodium Dithionite and [FeFe] Hydrogenase: Influence on the Enzyme Mechanism. *J. Am. Chem. Soc.* **2021**, *143* (43), 18159−18171.
(38) Rodríguez-Maciá, P.; Galle, L. M.; Bjornsson, R.; Lorent, C.; Zebger, I.; Yoda, Y.; Cramer, S. P.; DeBeer, S.; Span, I.; Birrell, J. A. Caught in the Hinact: Crystal Structure and Spectroscopy Reveal a Sulfur Bound to the Active Site of an O2-stable State of [FeFe] Hydrogenase. *Angew. Chem., Int. Ed.* **2020**, *59* (38), 16786−16794.
(39) Rutz, A.; Das, C. K.; Fasano, A.; Jaenecke, J.; Yadav, S.; Apfel, U.-P.; Engelbrecht, V.; Fourmond, V.; Léger, C.; Schäfer, L. V. Increasing the O2 resistance of the [FeFe]-hydrogenase Cba5h through enhanced protein flexibility. *ACS Catal.* **2022**, *13* (2), 856−865.
(40) Martini, M. A.; Bikbaev, K.; Pang, Y.; Lorent, C.; Wiemann, C.; Breuer, N.; Zebger, I.; DeBeer, S.; Span, I.; Bjornsson, R.; Birrell, J. A.; Rodríguez-Maciá, P. Binding of exogenous cyanide reveals new active-site states in [FeFe] hydrogenases. *Chem. Sci.* **2023**, *14* (11), 2826−2838.
(41) King, P. W.; Posewitz, M. C.; Ghirardi, M. L.; Seibert, M. Functional Studies of [FeFe] Hydrogenase Maturation in an < i > Escherichia coli</i> Biosynthetic System. *J. Bacteriol.* **2006**, *188* (6), 2163−2172.
(42) Mulder, D. W.; Ratzloff, M. W.; Bruschi, M.; Greco, C.; Koonce, E.; Peters, J. W.; King, P. W. Investigations on the Role of Proton-Coupled Electron Transfer in Hydrogen Activation by [FeFe]-Hydrogenase. *J. Am. Chem. Soc.* **2014**, *136* (43), 15394−15402.
(43) Mulder, D. W.; Ratzloff, M. W.; Shepard, E. M.; Byer, A. S.; Noone, S. M.; Peters, J. W.; Broderick, J. B.; King, P. W. EPR and FTIR Analysis of the Mechanism of H2 Activation by [FeFe]-Hydrogenase HydA1 from *Chlamydomonas reinhardtii*. *J. Am. Chem. Soc.* **2013**, *135* (18), 6921−6929.
(44) Posewitz, M. C.; King, P. W.; Smolinski, S. L.; Zhang, L.; Seibert, M.; Ghirardi, M. L. Discovery of two novel radical S-adenosylmethionine proteins required for the assembly of an active [Fe] hydrogenase. *J. Biol. Chem.* **2004**, *279* (24), 25711−25720.
(45) Böck, A.; King, P. W.; Blokesch, M.; Posewitz, M. C. Maturation of hydrogenases. *Adv. Microb. Physiol.* **2006**, *51*, 1−225.
(46) Kuchenreuther, J. M.; Britt, R. D.; Swartz, J. R. New Insights into [FeFe] Hydrogenase Activation and Maturase Function. *PLoS One* **2012**, *7* (9), No. e45850.

https://doi.org/10.1021/acs.biochem.5c00066
Biochemistry 2025, 64, 2455−2466

(47) Shepard, E. M.; Mus, F.; Betz, J. N.; Byer, A. S.; Duffus, B. R.; Peters, J. W.; Broderick, J. B. [FeFe]-Hydrogenase Maturation. *Biochemistry* **2014**, *53* (25), 4090−4104.
(48) Yu, X.; Rao, G.; Britt, R. D.; Rauchfuss, T. B. Final Stages in the Biosynthesis of the [FeFe]-Hydrogenase Active Site. *Angew. Chem., Int. Ed.* **2024**, *63* (22), No. e202404044.
(49) Jumper, J.; Evans, R.; Pritzel, A.; Green, T.; Figurnov, M.; Ronneberger, O.; Tunyasuvunakool, K.; Bates, R.; Žídek, A.; Potapenko, A.; Bridgland, A.; Meyer, C.; Kohl, S. A. A.; Ballard, A. J.; Cowie, A.; Romera-Paredes, B.; Nikolov, S.; Jain, R.; Adler, J.; Back, T.; Petersen, S.; Reiman, D.; Clancy, E.; Zielinski, M.; Steinegger, M.; Pacholska, M.; Berghammer, T.; Bodenstein, S.; Silver, D.; Vinyals, O.; Senior, A. W.; Kavukcuoglu, K.; Kohli, P.; Hassabis, D. Highly accurate protein structure prediction with AlphaFold. *Nature* **2021**, *596* (7873), 583−589.
(50) Varadi, M.; Anyango, S.; Deshpande, M.; Nair, S.; Natassia, C.; Yordanova, G.; Yuan, D.; Stroe, O.; Wood, G.; Laydon, A.; Žídek, A.; Green, T.; Tunyasuvunakool, K.; Petersen, S.; Jumper, J.; Clancy, E.; Green, R.; Vora, A.; Lutfi, M.; Figurnov, M.; Cowie, A.; Hobbs, N.; Kohli, P.; Kleywegt, G.; Birney, E.; Hassabis, D.; Velankar, S. AlphaFold Protein Structure Database: massively expanding the structural coverage of protein-sequence space with high-accuracy models. *Nucleic Acids Res.* **2022**, *50* (D1), D439−D444.
(51) Hekkelman, M. L.; de Vries, I.; Joosten, R. P.; Perrakis, A. AlphaFill: enriching AlphaFold models with ligands and cofactors. *Nat. Methods* **2023**, *20* (2), 205−213.
(52) Pandey, A. S.; Harris, T. V.; Giles, L. J.; Peters, J. W.; Szilagyi, R. K. Dithiomethylether as a Ligand in the Hydrogenase H-Cluster. *J. Am. Chem. Soc.* **2008**, *130* (13), 4533−4540.
(53) Ratzloff, M. W.; Wilker, M. B.; Mulder, D. W.; Lubner, C. E.; Hamby, H.; Brown, K. A.; Dukovic, G.; King, P. W. Activation Thermodynamics and H/D Kinetic Isotope Effect of the Hox to HredH+ Transition in [FeFe] Hydrogenase. *J. Am. Chem. Soc.* **2017**, *139* (37), 12879−12882.
(54) Stoll, S.; Schweiger, A. EasySpin, a comprehensive software package for spectral simulation and analysis in EPR. *J. Magn. Reson.* **2006**, *178* (1), 42−55.
(55) Hagedoorn, P. L.; van der Weel, L.; Hagen, W. R. EPR monitored redox titration of the cofactors of Saccharomyces cerevisiae Nar1. *J. Vis Exp* **2014**, No. 93, No. e51611.
(56) Albracht, S. P. J.; Roseboom, W.; Hatchikian, E. C. The active site of the [FeFe]-hydrogenase from *Desulfovibrio desulfuricans*. I. Light sensitivity and magnetic hyperfine interactions as observed by electron paramagnetic resonance. *JBIC, J. Biol. Inorg. Chem.* **2006**, *11* (1), 88−101.
(57) Mulder, D. W.; Guo, Y.; Ratzloff, M. W.; King, P. W. Identification of a Catalytic Iron-Hydride at the H-Cluster of [FeFe]-Hydrogenase. *J. Am. Chem. Soc.* **2017**, *139* (1), 83−86.
(58) Winkler, M.; Senger, M.; Duan, J.; Esselborn, J.; Wittkamp, F.; Hofmann, E.; Apfel, U.-P.; Stripp, S. T.; Happe, T. Accumulating the hydride state in the catalytic cycle of [FeFe]-hydrogenases. *Nat. Commun.* **2017**, *8* (1), No. 16115.
(59) Adamska, A.; Silakov, A.; Lambertz, C.; Rüdiger, O.; Happe, T.; Reijerse, E.; Lubitz, W. Identification and Characterization of the "Super-Reduced" State of the H-Cluster in [FeFe] Hydrogenase: A New Building Block for the Catalytic Cycle? *Angew. Chem., Int. Ed.* **2012**, *51* (46), 11458−11462.
(60) Ratzloff, M. W.; Artz, J. H.; Mulder, D. W.; Collins, R. T.; Furtak, T. E.; King, P. W. CO-Bridged H-Cluster Intermediates in the Catalytic Mechanism of [FeFe]-Hydrogenase CaI. *J. Am. Chem. Soc.* **2018**, *140* (24), 7623−7628.
(61) Silakov, A.; Kamp, C.; Reijerse, E.; Happe, T.; Lubitz, W. Spectroelectrochemical Characterization of the Active Site of the [FeFe] Hydrogenase HydA1 from *Chlamydomonas reinhardtii*. *Biochemistry* **2009**, *48* (33), 7780−7786.
(62) Lorent, C.; Katz, S.; Duan, J.; Kulka, C. J.; Caserta, G.; Teutloff, C.; Yadav, S.; Apfel, U.-P.; Winkler, M.; Happe, T.; Horch, M.; Zebger, I. Shedding Light on Proton and Electron Dynamics in [FeFe] Hydrogenases. *J. Am. Chem. Soc.* **2020**, *142* (12), 5493−5497.
(63) Katz, S.; Noth, J.; Horch, M.; Shafaat, H.; Happe, T.; Hildebrandt, P.; Zebger, I. Vibrational spectroscopy reveals the initial steps of biological hydrogen evolution. *Chem. Sci.* **2016**, *7* (11), 6746−6752.
(64) Sommer, C.; Adamska-Venkatesh, A.; Pawlak, K.; Birrell, J. A.; Rüdiger, O.; Reijerse, E. J.; Lubitz, W. Proton coupled electronic rearrangement within the H-cluster as an essential step in the catalytic cycle of [FeFe] hydrogenases. *J. Am. Chem. Soc.* **2017**, *139* (4), 1440−1443.
(65) Adamska-Venkatesh, A.; Krawietz, D.; Siebel, J.; Weber, K.; Happe, T.; Reijerse, E.; Lubitz, W. New redox states observed in [FeFe] hydrogenases reveal redox coupling within the H-cluster. *J. Am. Chem. Soc.* **2014**, *136* (32), 11339−11346.
(66) Birrell, J. A.; Pelmenschikov, V.; Mishra, N.; Wang, H.; Yoda, Y.; Tamasaku, K.; Rauchfuss, T. B.; Cramer, S. P.; Lubitz, W.; DeBeer, S. Spectroscopic and Computational Evidence that [FeFe] Hydrogenases Operate Exclusively with CO-Bridged Intermediates. *J. Am. Chem. Soc.* **2020**, *142* (1), 222−232.
(67) van der Vlugt, J. I.; Rauchfuss, T. B.; Whaley, C. M.; Wilson, S. R. Characterization of a Diferrous Terminal Hydride Mechanistically Relevant to the Fe-Only Hydrogenases. *J. Am. Chem. Soc.* **2005**, *127* (46), 16012−16013.
(68) Artz, J. H.; Mulder, D. W.; Ratzloff, M. W.; Lubner, C. E.; Zadvornyy, O. A.; LeVan, A. X.; Williams, S. G.; Adams, M. W. W.; Jones, A. K.; King, P. W.; Peters, J. W. Reduction Potentials of [FeFe]-Hydrogenase Accessory Iron−Sulfur Clusters Provide Insights into the Energetics of Proton Reduction Catalysis. *J. Am. Chem. Soc.* **2017**, *139* (28), 9544−9550.
(69) Land, H.; Ceccaldi, P.; Mészáros, L. S.; Lorenzi, M.; Redman, H. J.; Senger, M.; Stripp, S. T.; Berggren, G. Discovery of novel [FeFe]-hydrogenases for biocatalytic H 2-production. *Chem. Sci.* **2019**, *10* (43), 9941−9948.
(70) Lemon, B. J.; Peters, J. W. Photochemistry at the Active Site of the Carbon Monoxide Inhibited Form of the Iron-Only Hydrogenase (CpI). *J. Am. Chem. Soc.* **2000**, *122* (15), 3793−3794.
(71) Fried, S. D.; Boxer, S. G. Electric Fields and Enzyme Catalysis. *Annu. Rev. Biochem.* **2017**, *86* (1), 387−415.
(72) Stephens, P. J.; Jollie, D. R.; Warshel, A. Protein Control of Redox Potentials of Iron−Sulfur Proteins. *Chem. Rev.* **1996**, *96* (7), 2491−2514.
(73) Warshel, A.; Levitt, M. Theoretical studies of enzymic reactions: Dielectric, electrostatic and steric stabilization of the carbonium ion in the reaction of lysozyme. *J. Mol. Biol.* **1976**, *103* (2), 227−249.

https://doi.org/10.1021/acs.biochem.5c00066
Biochemistry 2025, 64, 2455−2466